Letter   Editors' Suggestion

Topological diffusive metal in amorphous transition metal monosilicides

Selma Franca [*] and Adolfo G. Grushin [†]

Université Grenoble Alpes, CNRS, Grenoble INP, Institut Néel, 38000 Grenoble, France

In chiral crystals crystalline symmetries can protect multifold fermions, pseudorelativistic masless quasiparticles that have no high-energy counterparts. Their realization in transition metal monosilicides has exemplified their intriguing physical properties, such as long Fermi arc surface states and unusual optical responses. Recent experimental studies on amorphous transition metal monosilicides suggest that topological properties may survive beyond crystals, even though theoretical evidence is lacking. Motivated by these findings, we theoretically study a tight-binding model of amorphous transition metal monosilicides. We find that topological properties of multifold fermions survive in the presence of structural disorder that converts the semimetal into a diffusive metal. We characterize this topological diffusive metal phase with the spectral localizer, a real-space topological indicator that we show can signal multifold fermions. Our findings showcase how topological properties can survive in disordered metals, and how they can be uncovered using the spectral localizer.

Introduction. Crystalline topological metals host quasiparticles classified according to the symmetries required to protect them. For example, Weyl semimetals require no symmetries to realize Weyl quasiparticles, which are spin-half, gapless low-energy quasiparticles governed by the Weyl equation [1]. Weyl bands disperse linearly around a two-band crossing point, accompanied by a quantized flux of Berry curvature, known as the monopole charge. The absence of symmetry requirements endows Weyl points with a relative robustness against disorder [2–20], explaining why they have been predicted to survive even in noncrystalline lattices [21].

Higher-spin generalizations of Weyl quasiparticles known as multifold fermions, predicted and observed in chiral crystals [22–31], seem more delicate. Their bands disperse linearly around multiband crossing points and can have an associated monopole charge. However, in contrast to Weyl quasiparticles, they require crystalline symmetries to ensure their robustness. The effect of disorder on multifold semimetals is much less explored [32,33], and it seems paradoxical that topology can survive the absence of long-range lattice order.

In this work we investigate to what extent the above expectation holds in a noncrystalline amorphous model. Our main result is that topological properties of multifold fermions can survive the absence of crystal symmetry. Recently, amorphous insulators have been predicted and observed to display topological phases, owing to the finite energy scale endowed by the gap [34–47]. Indeed, models of amorphous Chern insulators [34–36,38–40], quantum spin-Hall insulators [41–44], and three-dimensional topological insulators [34,45,46] demonstrate that topology survives the amorphicity and can even be induced by it [43]. Moreover,

average crystalline symmetries can also protect amorphous topological states, provided that the disorder strength is smaller than the band gap [48–52].

In turn, the survival of topology in amorphous metals is much more challenging to address due to the absence of a gap. Methods to detect metallic topology in real-space are scarce, especially in the presence of time-reversal symmetry where local Chern markers [53,54] are identically zero.

To make progress, here we amorphisize a known crystalline model of a chiral crystal in space group 198 [24,27,55,56]. Materials in this space group, such as the transition metal monosilicides RhSi or CoSi, lack inversion and mirror symmetries yet exhibit nonsymmorphic symmetries. These materials manifest exotic physical properties such as multifold fermions at the Fermi level, long Fermi arc surface states [55], a quantized circular photogalvanic effect [31,55,57–60], and unusual magnetotransport features [23,55,61,62]. Moreover, a recent experimental study on amorphous CoSi (a-CoSi) has found a range of intriguing magnetotransport properties [63].

Using the recently introduced spectral localizer [64–69], we find that multifold fermions enter a topological diffusive metal (TDM) phase in the presence of moderate structural disorder. We find that localizer in-gap modes can be traced back to the existence of multifold fermions and coexisting with spectral properties characteristic of a diffusive metal [13]. Upon increasing disorder, the localizer in-gap modes are lost, leaving behind a trivial diffusive metal (DM) that eventually localizes into a trivial Anderson insulator (AI). Using the spectral localizer to define TDMs can be extended to any symmetry class and hence is the main result of this work [see Fig. 1(a)].

Model Hamiltonian. Amorphous systems lack long-range order, but they display short-range ordering, dictated by the local chemistry of the elements [70]. This implies the existence of preferred bond lengths and angles peaked around the

*selma.franca@neel.cnrs.fr
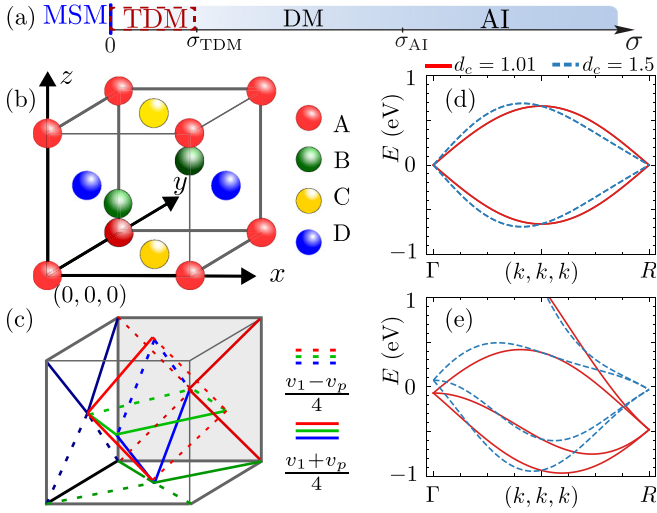†adolfo.grushin@neel.cnrs.fr

FIG. 1. (a) Schematic phase diagram found in this work, including the multifold semimetal (MSM), the topological diffusive metal (TDM), the diffusive metal (DM), and the Anderson insulator (AI) phases, as a function of the disorder variance σ. The TDM persists until σ_{TDM} that is defined in Fig. 4 and is signaled by in-gap states of the localizer as well as a finite DOS at E_F typical of a diffusive metal. The trivial DM phase is delimited by σ_{AI}, defined in Fig. 3, from the AI phase. (b) Orbitals of the crystalline unit cell. (c) The nearest-neighbor interorbital hoppings $\frac{v_1 \pm v_p}{4}$ represented by solid and dashed lines. The color denotes hoppings between different sets of orbitals: red for A-B/C-D, blue for A-D/B-C, and green for A-C/B-D. (d) Band structure for parameter regime (i) with $v_1 = v_2 = 0$ and $v_p = -0.762$. (e) Band structure for parameter regime (ii), a-RhSi, with $v_1 = 0.55$, $v_2 = 0.16$, and $v_p = -0.762$. Solid and dashed curves correspond to maximum hopping radii $d_c = 1.01$ and 1.5, respectively. In panel (d), the spectrum is doubly degenerate with two double-Weyl fermions occurring at Γ and R points. In panel (e), a-RhSi regime, we see a threefold fermion at the Γ point and a double-Weyl fermion at the R point.

crystalline values [71–73]. Hence, we first revisit the crystalline model of RhSi and CoSi, in space group 198, on which we base our amorphous model. This space group has three nonintersecting twofold screw symmetries $s_{2x,y,z}$ and a diagonal cubic threefold rotation $C_{3,111}$. The spin-orbit coupling in RhSi [55] and CoSi [74] is weak (tens of millielectron volts), and is neglected in our simulations. In this case, the band structure near the Fermi level is captured by a tight-binding Hamiltonian with four s-type orbitals (A, B, C, D) positioned at $(0,0,0)$, $(\frac{a}{2}, 0, \frac{a}{2})$, $(\frac{a}{2}, \frac{a}{2}, 0)$, and $(0, \frac{a}{2}, \frac{a}{2})$ [see Fig. 1(b)] [55]. In the following, we measure all distances in units of a. Nearest-neighboring orbitals are connected by interorbital hoppings while second nearest-neighbors are connected via intraorbital hoppings. Figure 1(c) illustrates the interorbital hoppings within the unit cell, which take two values $(v_1 \pm v_p)/4$, depending on the bond orientation. The amplitude $v_2/2$ of intraorbital hoppings is independent of the bond orientation. The Bloch Hamiltonian is discussed further in the Supplemental Material (SM) [75].

It is convenient to consider two parameter regimes, expressed in electron volts: (i) when only $v_p = -0.762$ is nonzero, and (ii) when $v_1 = 0.55$, $v_2 = 0.16$, and

$v_p = -0.762$ eV. The hopping amplitudes in regime (ii) are chosen such that the crystalline tight-binding Hamiltonian [75] reproduces well the density-functional theory calculated band structure of RhSi near the Fermi level [55]. Hence, in the following we refer to regime (ii) as a-RhSi regime. The red curves in Figs. 1(d) and 1(e) show bulk spectra for the two regimes, respectively. In regime (i), the spectrum is doubly degenerate in the entire Brillouin zone and features two double-Weyl fermions, one at the Γ point and one at the R point, occurring at the same energy $E = 0$. In the a-RhSi regime, v_1 and v_2 turn the double-Weyl fermion at Γ into a threefold fermion, energetically shifted with respect to the double-Weyl fermion at the R point. In both regimes, the crossings at Γ and R have monopole charges $C = 2$ and -2, respectively.

We create the amorphous lattice by displacing every site n (representing a single orbital) of crystalline RhSi by $\delta \mathbf{r}_n = (\delta x_n, \delta y_n, \delta z_n)$ drawn from a Gaussian distribution:

$$D(\delta \mathbf{r}_n) = \frac{1}{2\pi\sigma^2} \exp\left[-\frac{|\delta \mathbf{r}_n|^2}{2\sigma^2}\right]. \tag{1}$$

The variance σ^2 is typically proportional to the quenching temperature to form the amorphous solid, $\sigma^2 \propto k_B T$ [43]. To avoid artificial clustering of sites, we impose a minimal distance of $d_{\min} = 0.4$ [48]. The possible hoppings $\tilde{v}_\alpha$ ($\alpha = 1$, 2, and p) between sites at positions $\mathbf{r}_n = (x_n, y_n, z_n)$ and $\mathbf{r}_m = (x_m, y_m, z_m)$ are determined from

$$\tilde{v}_\alpha = \tilde{v}_\alpha(d)\tilde{v}_\alpha(\theta, \phi) \exp\left[1 - \frac{d}{d_\alpha^0}\right]\Theta(d_c - d), \tag{2}$$

in spherical coordinates (d, θ, ϕ) with $d = |\mathbf{r}_n - \mathbf{r}_m|$. Here, d_α^0 depends on whether the hopping is interorbital, where $d_1^0 = d_p^0 = 1/\sqrt{2}$, or intraorbital, where $d_2^0 = 1$.

Since the intraorbital hopping $v_2/2$ of crystalline RhSi is independent of bond orientation [75], we take $\tilde{v}_2(\theta, \phi) = 1$ and $\tilde{v}_2(d) = v_2/d$. The interorbital hopping of crystalline RhSi has amplitude $(v_1 \pm v_p)/4$ [see Fig. 1(c)], where the hopping v_p is direction dependent, unlike v_1. Hence, we take $\tilde{v}_1(\theta, \phi) = 1$, $\tilde{v}_1(d) = v_1/\sqrt{2}d$, and $\tilde{v}_p(d) = v_p/d$. In contrast, the hopping $\tilde{v}_p(\theta, \phi)$ depends on the type of orbitals that form the bond as detailed in the SM [75]. The hopping $\tilde{v}_\alpha$ recovers the original tight-binding Hamiltonian in the crystalline limit when $\sigma \to 0$ [55,75].

The step function Θ in Eq. (2) ensures that the maximum distance between two sites is d_c, whose effect is shown in Figs. 1(d) and 1(e). Notably for a-RhSi longer-range hoppings reduce the energy difference between threefold and double-Weyl fermions. In our simulations, $d_c = 1.5$, which allows one to account for longer-range hoppings [see SM [75]].

Lastly, to account for possible potential disorder [48], we add random on-site potentials drawn from the Gaussian distribution Eq. (1). Thus, our model accounts for all types of disorder expected in amorphous solids: on-site, hopping, and structural disorder.

Spectral properties. The density of states (DOS) characterizes disordered topological semimetals [15] and can be defined as $\rho^\lambda(E) = \frac{1}{V} \sum_m \delta(E - E_m)$, where λ labels a disorder realization, m runs over all states of the system, and $V = 4L^3$ for a cubic system with L unit cells in each direction.
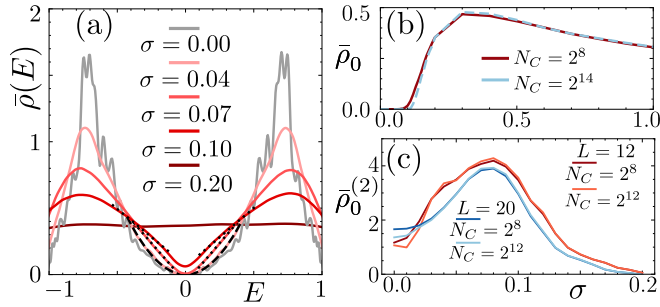
FIG. 2. (a) $\rho(E)$ vs E as a function of σ. Dashed and dotted lines represent fit functions αE^2 and $\alpha + \beta|E|$, respectively. (b) The averaged zero-energy DOS $\bar{\rho}_0$ as a function of disorder strength σ; ρ_0 becomes nonzero at $\sigma \approx 0.1$. (c) $\bar{\rho}^{(2)}(0)$ vs σ peaks around $\sigma_c = 0.08$ independent of system size ($L = 12$ and 20) and KPM order N_C. We define $\bar{\rho}^{(2)}(0) = \sum_{\lambda=1}^{N_{\text{dis}}} (\rho^\lambda)^{(2)}(0)$, where $(\rho^\lambda)^{(2)}(0)$ is estimated from a fit $\rho^\lambda(E) = \rho_0^\lambda + (\rho^\lambda)^{(2)}(0)E^2$ in the energy range $(-0.2, 0.2)$ for independent disorder realizations λ.

For every disorder realization, the DOS is calculated using the numerically efficient kernel polynomial method (KPM), which relies on a Chebyshev polynomial expansion up to order N_C [76]. In the following, we study the disorder-averaged DOS $\bar{\rho}(E) = \frac{1}{N_{\text{dis}}} \sum_{\lambda=1}^{N_{\text{dis}}} \rho^\lambda(E)$, with $N_{\text{dis}} = 16$.

We focus first on regime (i) that has two double-Weyl fermions at $E = 0$ in the crystalline limit. Figures 2(a) and 2(b) show $\bar{\rho}(E)$ for different disorder strengths and $\bar{\rho}_0 \equiv \bar{\rho}(E = 0)$ for different KPM orders N_C, respectively. We see that for $\sigma \lesssim 0.04$, $\bar{\rho}(E) \to |E|^2$, as in periodic systems with (double-)Weyl fermions at the same energy. Once the disorder strength is increased up to $\sigma \approx 0.07$, $\bar{\rho} \propto |E|$ close to $E = 0$. Additionally, at $\sigma = 0.1$ the DOS at $E = 0$ becomes nonzero. Figure 2(b) reveals that $\bar{\rho}_0 \neq 0$ for $\sigma \geqslant 0.1$ signaling that the system becomes a diffusive metal, a phase with constant DOS in a range of energies.

This behavior suggests a putative quantum critical point (QCP) at a certain σ_c, where the semimetal phase is replaced by a diffusive metal [13,16]. To study this phase transition in more detail, Fig. 2(c) shows $\bar{\rho}_0^{(2)}$, extracted from a low-energy fit $\bar{\rho}(E) = \bar{\rho}_0 + \bar{\rho}_0^{(2)}E^2$ to the DOS [13]. It remains finite with a maximum at $\sigma_c \approx 0.08$, which shifts little with increasing system size or the order of the KPM expansion. This nondivergent behavior signals that the putative QCP is avoided [13].

Avoiding such a QCP is enabled by the presence of statistically rare states [13]. Rare states are low-energy eigenstates that are quasibounded to the real-space regions with uncharacteristically large potential strengths that are statistically rare. In the thermodynamic limit, these statistically rare events are likely to occur for any nonzero σ. As a result, $\bar{\rho}_0$ becomes exponentially small in disorder strength but nonzero, implying a crossover from a semimetal phase to a diffusive metal phase instead of a perturbative transition [13,16] [see SM [75] for more details].

Importantly, it is the vanishing DOS at the band crossing that makes rare states dominate the physics of disordered Weyl semimetals. The DOS vanishes at $E = 0$ for parameter regime (i), where two Weyl nodes coexist at the Fermi level, but not

for the a-RhSi regime (ii). In the latter, disorder can couple states without energy penalty [77], turning the a-RhSi regime into a diffusive metal for any infinitesimal amount of disorder.

Anderson localization. While eigenstates of diffusive metals are extended, sufficiently strong disorder will turn metallic systems into Anderson insulators with localized eigenstates [15]. Localized states interact weakly, thus producing an uncorrelated energy spectrum that obeys a Poisson distribution function [78]. On the metallic side, the overlap of delocalized states leads to the repulsion of associated energy levels. For spinless and time-reversal symmetric systems, like a-RhSi, such a spectrum falls under the Gaussian orthogonal ensemble (GOE) of random matrices [79].

To distinguish between metallic and insulating regimes, we calculate the adjacent energy level spacing ratio and the inverse participation ratio (IPR) of states at the Fermi level E_F. The adjacent level spacing ratio is defined as

$$r = \frac{1}{N_E - 2} \sum_m \frac{\min(\tilde{E}_{m,m-1}, \tilde{E}_{m+1,m})}{\max(\tilde{E}_{m,m-1}, \tilde{E}_{m+1,m})}, \qquad (3)$$

where $\tilde{E}_{m,n} = E_m - E_n$ and the energy levels are arranged such that $E_m > E_{m-1}$. The sum is performed over N_E energy levels within the interval $[E_F - \Delta E, E_F + \Delta E]$. The GOE and Poisson spectra have $r_{\text{GOE}} \approx 0.54$ and $r_P \approx 0.39$, respectively [80]. To quantify the localization of a set of eigenstates near E_F, we use the IPR defined as IPR $= \sum_m \sum_{\mathbf{r}_n} |\Psi_m(\mathbf{r}_n)|^4 / N_E$. Here Ψ_m is the eigenstate corresponding to the mth eigenvalue, and the sum is taken over the same energy window $[E_F - \Delta E, E_F + \Delta E]$ as for r. The IPR is close to zero (unity) for delocalized (localized) states.

In the following, we focus on small system sizes $L = 6, 8$, and 10 where exact diagonalization is possible. We fix $E_F = 0$ and $\Delta E = 0.1$ in order to probe the physics near the multifold crossings, and we calculate the disorder-averaged r and IPR: $\bar{r}$ ($\overline{\text{IPR}}$) $= \frac{1}{N_{\text{dis}}} \sum_{\lambda=1}^{N_{\text{dis}}} r^\lambda$ (IPR^λ), where $N_{\text{dis}} = 101$. The results are shown in Figs. 3(a) and 3(b) for the parameter regime (i) and the a-RhSi regime, respectively. In both cases, we observe that the transition from $\bar{r} \approx 0.54$ (GOE) to $\bar{r} \approx 0.39$ (Poisson) occurs gradually due to finite-size effects, a behavior also reflected in the IPR that changes from 0 to ≈ 1 as σ is increased.

To find the disorder strength for which the topological phase transition into Anderson insulator phase occurs, we use the typical DOS at $E = 0$ defined as $\bar{\rho}_0^t = \exp[\sum_{\mathbf{r}_n} (\sum_{\lambda=1}^{N_{\text{dis}}} \log \rho_0^\lambda(\mathbf{r}_n)/N_{\text{dis}})/V_t]$. Here, $\rho_0^\lambda(\mathbf{r}_n)$ is the local DOS at site $\mathbf{r}_n$ and energy $E = 0$, while $V_t = 32$ is the total number of sites (eight sites in the bulk for each orbital type). We calculate the typical DOS for a system of linear size $L = 20$. Since the typical DOS is not a self-averaging quantity, we set the number of disorder realizations to $N_{\text{dis}} = 51$. The results are shown in Figs. 3(c) and 3(d) for regime (i) and the a-RhSi regime, respectively. The typical DOS is sensitive in the order of the KPM expansion N_C [15], and to determine σ_{AI} we extrapolate ρ_0^t to zero using the Richardson extrapolation method for data points obtained with $N_C = 2^{14}$. We obtain $\sigma_{\text{AI}} = 2.715$ for regime (i) and $\sigma_{\text{AI}} = 2.985$ for the a-RhSi regime.

Topological phase diagram. Lastly, we are interested in quantifying to what extent the topological properties of
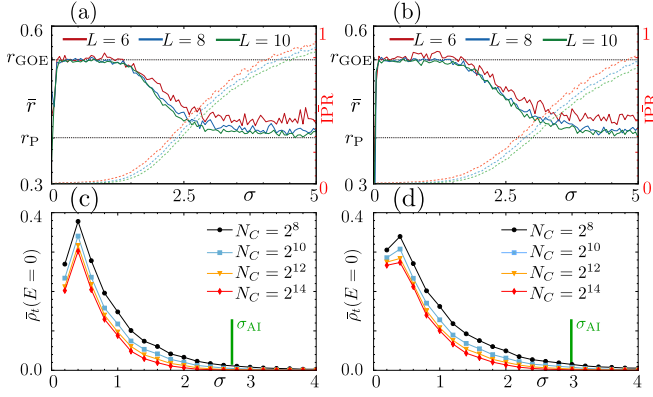
FIG. 3. Panels (a) and (b) show disorder-averaged adjacent level spacing ratios (solid lines) and inverse participation ratios (dashed lines) at $E_F = 0$ as a function of disorder strength σ for a system in parameter regime (i) and the a-RhSi regime, respectively. Panels (c) and (d) show the disorder-averaged typical DOS for different orders of the KPM expansion N_C as a function of σ for a system in parameter regime (i) and the a-RhSi regime, respectively. Here, σ_{AI} is the critical disorder strength at which the system transitions from a DM phase to an AI phase.

multifold fermions survive disorder. In time-reversal symmetric systems like RhSi, we cannot use real-space invariants like the local Chern marker [54] or the Bott index [53], used for time-reversal breaking Weyl semimetals [21,81]. Instead, we resort to the recently introduced spectral localizer [67–69].

In three dimensions, the spectral localizer is defined as [67,69]

$$\mathcal{L}(\mathbf{r}, E) = \kappa \sum_{j=1}^{3} \gamma_j (X_j - x_j \mathbb{1}) + \gamma_4 (H - E \mathbb{1}), \qquad (4)$$

where X_j are position operators corresponding to the Hamiltonian H, and the matrices γ_j form a Clifford representation $\{\gamma_j, \gamma_i\} = 2\delta_{ij}$. We choose $\gamma_j = \tau_z \sigma_j$ for $j = 1$, 2, and 3 and $\gamma_4 = \tau_x \sigma_0$, where σ_j and τ_j are Pauli matrices. The coefficient κ fixes the units and relative weights between X_j and H [65,69]; see also the SM [75] for a discussion concerning different values of κ. While the spectral localizer can be evaluated at any position $\mathbf{r}$ and energy E, here we choose $\mathbf{r}$ to be at the center of our system ($\mathbf{r} = \mathbf{0} \rightarrow x_j = 0 \; \forall j$) in order to probe the bulk properties at $E = 0$. In the following, we abbreviate $\mathcal{L}(\mathbf{0}, 0)$ with $\mathcal{L}_0$.

The spectrum of $\mathcal{L}_0$ consists of pairs $(\epsilon, -\epsilon)$ because $\mathcal{L}_0$ obeys chiral symmetry $\mathcal{C} = \tau_y \sigma_0 \mathbb{1}$. In the crystalline limit, the parameter regime (i) yields four states pinned at $\epsilon = 0$, which are separated from the remaining states by a gap of order $\sqrt{\kappa}$. Using a semiclassical analysis of the operator $\mathcal{L}_0^2$ [68,75], it is possible to show analytically that each Weyl node contributes exactly one zero mode [68]. We have generalized such an analysis [75] for the case of a system with threefold and double-Weyl fermions, i.e., the a-RhSi regime, predicting four midgap modes as well [75]. The number of midgap modes of $\mathcal{L}_0$ can be thus used to signal multifold fermions in both regimes, as trivial metals present different midgap mode counting [82].

To study how $\mathcal{L}_0$ changes with disorder, we focus on its DOS $\rho_{\mathcal{L}_0}$, calculated using the KPM [76] with an energy
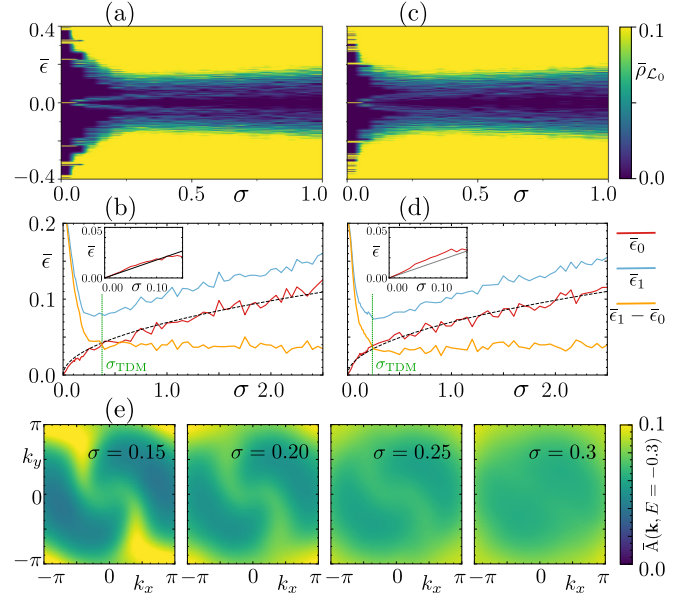

FIG. 4. Panels (a) and (c) show $\bar{\rho}_{\mathcal{L}_0}$—the disorder-averaged DOS of the operator $\mathcal{L}_0$ as a function of disorder strength σ for regime (i) and the a-RhSi regime, respectively. In panels (b) and (d) are plotted disorder-averaged energies of the midgap and first-excited states $\bar{\epsilon}_0$ and $\bar{\epsilon}_1$ and their difference $\bar{\epsilon}_1 - \bar{\epsilon}_0$ as a function of σ for the two parameter regimes. Here, dashed green lines represent the topological phase transition point σ_{TDM} at which $\bar{\epsilon}_1 \approx 2\bar{\epsilon}_0$. The dashed black line represents a fit $\bar{\epsilon}_0 = a\sqrt{\sigma}$, where $a = 0.0692$ in regime (i) and $a = 0.0696$ in regime (ii). The insets of panels (b) and (d) show how well $\bar{\epsilon}_0$ matches with the predicted form $\kappa^{0.75}\sigma$ [68] (gray line) in the case of small disorder strengths. For panels (a)–(d), we consider $\kappa = 0.1$ and $N_{\mathrm{dis}} = 25$. In panel (e) are plotted disorder-averaged ($N_{\mathrm{dis}} = 10$) momentum-resolved spectral functions $\bar{A}(\mathbf{k}, E = -0.3)$ for different disorder strengths σ.

resolution of $\Delta\epsilon = 5 \times 10^{-4}$ ($N_C \sim 6000$). The system size is $L = 12$ and we consider $N_{\mathrm{dis}} = 25$ disorder realizations. Figure 4(a) shows the disorder-averaged DOS $\bar{\rho}_{\mathcal{L}_0}$, as a function of disorder strength σ for regime (i). From Fig. 4(a), we see that as σ is increased, the four zero-energy states split into a pair of peaks that move away from $\epsilon = 0$ in a symmetric fashion. In parallel, disorder reduces the spectral localizer gap and, at around $\sigma_{\mathrm{TDM}} = 0.35$, the energies of the midgap and first-excited states become comparable, indicating the transition into a trivial DM. The existence of the topological in-gap modes of $\mathcal{L}_0$ for $\sigma < \sigma_{\mathrm{TDM}}$ defines the topological diffusive metal phase [see Fig. 1(a)].

The transition from a TDM to a trivial DM is also apparent by tracking, for every disorder realization λ, the peak positions ϵ_0^λ and ϵ_1^λ corresponding to the midgap mode and the first-excited state, respectively. In Fig. 4(b), we plot disorder-averaged energies $\bar{\epsilon}_{0,1} = \frac{1}{N_{\mathrm{dis}}} \sum_{\lambda=1}^{N_{\mathrm{dis}}} \epsilon_{0,1}^\lambda$ as a function of σ. We see that $\bar{\epsilon}_0$ and $\bar{\epsilon}_1$ approach each other for small disorder strengths, and without crossing each other they start to evolve together with stronger disorder, indicating a topologically trivial system. Since a topological phase is preserved with disorder as long as the dimensionality of the operator's $\mathcal{L}_0$ null space is nonzero, it is natural to assume that the topological

phase transition occurs when $\bar{\epsilon}_1 - \bar{\epsilon}_0 \approx \bar{\epsilon}_0 \rightarrow \bar{\epsilon}_1 \approx 2\bar{\epsilon}_0$. For parameter regime (i), this occurs for $\sigma_{\text{TDM}} \approx 0.35$.

In addition, for small disorder strengths, see inset of Fig. 4(b), we find that $\bar{\epsilon}_0 = \sigma\kappa^{3/4}$ consistent with the analytical prediction concerning weakly disordered Weyl semimetals [68]. Moreover, we find that $\bar{\epsilon}_0$ can be fitted with a function $a\sqrt{\sigma}$ ($a \approx 0.07$) in the entire disorder range.

In Figs. 4(c) and 4(d) we show results for the a-RhSi regime. Even though the system supports a threefold fermion in the crystalline limit, $\bar{\rho}_{\mathcal{L}_0}$ behaves similarly to regime (i) with two double-Weyl fermions. From Fig. 4(d), we see that $\sigma_{\text{TDM}} \approx 0.25$. Furthermore, we recover $\bar{\epsilon}_0 = \sigma\kappa^{3/4}$ behavior in the limit of small disorder, as well as $\bar{\epsilon}_0 \propto \sqrt{\sigma}$ for the entire disorder range.

To confirm that the spectral localizer correctly captures the topological phase transition, we study how the Fermi arcs at the top surface of a system in the a-RhSi regime evolve with disorder. These arcs can be seen with the disorder-averaged momentum-resolved spectral function $\bar{A}(\mathbf{k}, E = -0.3)$ that can be measured in angle-resolved photoemission experiments [83]. The plots of $\bar{A}(\mathbf{k}, E = -0.3)$ in Fig. 4(e) for disorder strengths $\sigma = 0.15$, 0.2, 0.25, and 0.3 indicate that the Fermi arcs disappear for $\sigma > 0.25$, in agreement with the prediction of $\mathcal{L}_0$. For more details, see the SM [75].

We find that both regimes behave similarly as long the hopping amplitude v_p is the largest energy scale. This condition ensures a sizable difference between the amplitudes of direction-dependent nearest-neighbor hoppings $(v_1 \pm v_p)/4$. This condition is met by the RhSi parameters but not by

those of CoSi, where the parameter v_1 is more than three times larger than the parameter v_p. As a result, the topological properties of a-CoSi are expected to be less robust compared to a-RhSi [75].

Conclusion. We have shown that a topological type of diffusive metal can exist in transition metal monosilicides in the presence of structural, potential, and hopping disorder. Characterizing this novel phase required us to extend the recently discovered spectral localizer $\mathcal{L}$ to accommodate multifold fermions. The spectral localizer can be used to signal TDMs in any symmetry class, including those for which other real-space methods yield trivial results or are ill-defined.

Our analysis highlights a-RhSi as a more robust platform than a-CoSi to realize the topological diffusive metal due to a larger anisotropy between nearest-neighbor hoppings. Looking forward, it is worth studying whether such stability permeates to physical properties such as the photogalvanic effect or negative magnetoresistance.

The KWANT code [84] used to generate our results is available from Ref. [85].

[1] N. P. Armitage, E. J. Mele, and A. Vishwanath, Weyl and Dirac semimetals in three-dimensional solids, Rev. Mod. Phys. **90**, 015001 (2018).

[2] E. Fradkin, Critical behavior of disordered degenerate semiconductors. I. Models, symmetries, and formalism, Phys. Rev. B **33**, 3257 (1986).

[3] E. Fradkin, Critical behavior of disordered degenerate semiconductors. II. Spectrum and transport properties in mean-field theory, Phys. Rev. B **33**, 3263 (1986).

[4] A. Altland and D. Bagrets, Effective field theory of the disordered Weyl semimetal, Phys. Rev. Lett. **114**, 257201 (2015).

[5] S. V. Syzranov, P. M. Ostrovsky, V. Gurarie, and L. Radzihovsky, Critical exponents at the unconventional disorder-driven transition in a Weyl semimetal, Phys. Rev. B **93**, 155113 (2016).

[6] J. H. Pixley, P. Goswami, and S. Das Sarma, Disorder-driven itinerant quantum criticality of three-dimensional massless Dirac fermions, Phys. Rev. B **93**, 085103 (2016).

[7] A. Altland and D. Bagrets, Theory of the strongly disordered Weyl semimetal, Phys. Rev. B **93**, 075113 (2016).

[8] B. Sbierski, K. S. C. Decker, and P. W. Brouwer, Weyl node with random vector potential, Phys. Rev. B **94**, 220202(R) (2016).

[9] T. Louvet, D. Carpentier, and A. A. Fedorenko, On the disorder-driven quantum transition in three-dimensional relativistic metals, Phys. Rev. B **94**, 220201(R) (2016).

[10] T. Louvet, D. Carpentier, and A. A. Fedorenko, New quantum transition in Weyl semimetals with correlated disorder, Phys. Rev. B **95**, 014204 (2017).

[11] X. Luo, B. Xu, T. Ohtsuki, and R. Shindou, Quantum multicriticality in disordered Weyl semimetals, Phys. Rev. B **97**, 045129 (2018).

[12] I. Balog, D. Carpentier, and A. A. Fedorenko, Disorder-driven quantum transition in relativistic semimetals: Functional renormalization via the porous medium equation, Phys. Rev. Lett. **121**, 166402 (2018).

[13] J. H. Pixley and J. H. Wilson, Rare regions and avoided quantum criticality in disordered Weyl semimetals and superconductors, Ann. Phys. **435**, 168455 (2021).

[14] R. Nandkishore, D. A. Huse, and S. L. Sondhi, Rare region effects dominate weakly disordered three-dimensional Dirac points, Phys. Rev. B **89**, 245110 (2014).

[15] J. H. Pixley, P. Goswami, and S. Das Sarma, Anderson localization and the quantum phase diagram of three dimensional disordered Dirac semimetals, Phys. Rev. Lett. **115**, 076601 (2015).

[16] J. H. Pixley, D. A. Huse, and S. Das Sarma, Rare-region-induced avoided quantum criticality in disordered three-dimensional Dirac and Weyl semimetals, Phys. Rev. X **6**, 021042 (2016).

[17] V. Gurarie, Theory of avoided criticality in quantum motion in a random potential in high dimensions, Phys. Rev. B **96**, 014205 (2017).

[18] M. Buchhold, S. Diehl, and A. Altland, Vanishing density of states in weakly disordered Weyl semimetals, Phys. Rev. Lett. **121**, 215301 (2018).

[19] M. Buchhold, S. Diehl, and A. Altland, Nodal points of Weyl semimetals survive the presence of moderate disorder, Phys. Rev. B **98**, 205134 (2018).

[20] J. H. Wilson, D. A. Huse, S. Das Sarma, and J. H. Pixley, Avoided quantum criticality in exact numerical simulations of a single disordered Weyl cone, Phys. Rev. B **102**, 100201(R) (2020).

[21] Y.-B. Yang, T. Qin, D.-L. Deng, L.-M. Duan, and Y. Xu, Topological amorphous metals, Phys. Rev. Lett. **123**, 076401 (2019).

[22] J. L. Mañes, Existence of bulk chiral fermions and crystal symmetry, Phys. Rev. B **85**, 155118 (2012).

[23] B. Bradlyn, J. Cano, Z. Wang, M. G. Vergniory, C. Felser, R. J. Cava, and B. A. Bernevig, Beyond Dirac and Weyl fermions: Unconventional quasiparticles in conventional crystals, Science **353**, aaf5037 (2016).

[24] P. Tang, Q. Zhou, and S.-C. Zhang, Multiple types of topological fermions in transition metal silicides, Phys. Rev. Lett. **119**, 206402 (2017).

[25] G. Chang, B. J. Wieder, F. Schindler, D. S. Sanchez, I. Belopolski, S.-M. Huang, B. Singh, D. Wu, T.-R. Chang, T. Neupert, S.-Y. Xu, H. Lin, and M. Z. Hasan, Topological quantum properties of chiral crystals, Nat. Mater. **17**, 978 (2018).

[26] D. S. Sanchez, I. Belopolski, T. A. Cochran, X. Xu, J.-X. Yin, G. Chang, W. Xie, K. Manna, V. Süß, C.-Y. Huang, N. Alidoust, D. Multer, S. S. Zhang, N. Shumiya, X. Wang, G.-Q. Wang, T.-R. Chang, C. Felser, S.-Y. Xu, S. Jia *et al.*, Topological chiral crystals with helicoid-arc quantum states, Nature (London) **567**, 500 (2019).

[27] D. Takane, Z. Wang, S. Souma, K. Nakayama, T. Nakamura, H. Oinuma, Y. Nakata, H. Iwasawa, C. Cacho, T. Kim, K. Horiba, H. Kumigashira, T. Takahashi, Y. Ando, and T. Sato, Observation of chiral fermions with a large topological charge and associated Fermi-arc surface states in CoSi, Phys. Rev. Lett. **122**, 076402 (2019).

[28] Z. Rao, H. Li, T. Zhang, S. Tian, C. Li, B. Fu, C. Tang, L. Wang, Z. Li, W. Fan, J. Li, Y. Huang, Z. Liu, Y. Long, C. Fang, H. Weng, Y. Shi, H. Lei, Y. Sun, T. Qian *et al.*, Observation of unconventional chiral fermions with long Fermi arcs in CoSi, Nature (London) **567**, 496 (2019).

[29] N. B. M. Schröter, D. Pei, M. G. Vergniory, Y. Sun, K. Manna, F. de Juan, J. A. Krieger, V. Süss, M. Schmidt, P. Dudin, B. Bradlyn, T. K. Kim, T. Schmitt, C. Cacho, C. Felser, V. N. Strocov, and Y. Chen, Chiral topological semimetal with multifold band crossings and long Fermi arcs, Nat. Phys. **15**, 759 (2019).

[30] D. S. Wu, Z. Y. Mi, Y. J. Li, W. Wu, P. L. Li, Y. T. Song, G. T. Liu, G. Li, and J. L. Luo, Single crystal growth and magnetoresistivity of topological semimetal CoSi, Chinese Phys. Lett. **36**, 077102 (2019).

[31] Z. Ni, K. Wang, Y. Zhang, O. Pozo, B. Xu, X. Han, K. Manna, J. Paglione, C. Felser, A. G. Grushin, F. de Juan, E. J. Mele, and L. Wu, Giant topological longitudinal circular photo-galvanic effect in the chiral multifold semimetal CoSi, Nat. Commun. **12**, 154 (2021).

[32] H.-C. Hsu, I. C. Fulga, and J.-S. You, Disorder effects on triple-point fermions, Phys. Rev. B **106**, 245118 (2022).

[33] R. Kikuchi and A. Yamakage, Electrical conductivity and screening effect of spin-1 chiral fermions scattered by charged impurities, Phys. Rev. B **108**, 085204 (2023).

[34] A. Agarwala and V. B. Shenoy, Topological insulators in amorphous systems, Phys. Rev. Lett. **118**, 236402 (2017).

[35] S. Mansha and Y. D. Chong, Robust edge states in amorphous gyromagnetic photonic lattices, Phys. Rev. B **96**, 121405(R) (2017).

[36] N. P. Mitchell, L. M. Nash, D. Hexner, A. M. Turner, and W. T. M. Irvine, Amorphous topological insulators constructed from random point sets, Nat. Phys. **14**, 380 (2018).

[37] G.-W. Chern, Topological insulator in an atomic liquid, Europhys. Lett. **126**, 37002 (2019).

[38] Q. Marsal, D. Varjas, and A. G. Grushin, Topological Weaire–Thorpe models of amorphous matter, Proc. Natl. Acad. Sci. USA **117**, 30260 (2020).

[39] I. Sahlberg, A. Weststrom, K. Pöyhönen, and T. Ojanen, Topological phase transitions in glassy quantum matter, Phys. Rev. Res. **2**, 013053 (2020).

[40] M. N. Ivaki, I. Sahlberg, and T. Ojanen, Criticality in amorphous topological matter: Beyond the universal scaling paradigm, Phys. Rev. Res. **2**, 043301 (2020).

[41] M. Costa, G. R. Schleder, M. Buongiorno Nardelli, C. Lewenkopf, and A. Fazzio, Toward realistic amorphous topological insulators, Nano Lett. **19**, 8941 (2019).

[42] B. Focassio, G. R. Schleder, M. Costa, A. Fazzio, and C. Lewenkopf, Structural and electronic properties of realistic two-dimensional amorphous topological insulators, 2D Mater. **8**, 025032 (2021).

[43] C. Wang, T. Cheng, Z. Liu, F. Liu, and H. Huang, Structural amorphization-induced topological order, Phys. Rev. Lett. **128**, 056401 (2022).

[44] J. Ma and H. Huang, Amorphous Kane-Mele model in disordered hyperuniform two-dimensional networks, Phys. Rev. B **106**, 195150 (2022).

[45] T. Mano and T. Ohtsuki, Application of convolutional neural network to quantum percolation in topological insulators, J. Phys. Soc. Jpn. **88**, 123704 (2019).

[46] P. Mukati, A. Agarwala, and S. Bhattacharjee, Topological and conventional phases of a three-dimensional electronic glass, Phys. Rev. B **101**, 035142 (2020).

[47] P. Corbae, S. Ciocys, D. Varjas, E. Kennedy, S. Zeltmann, M. Molina-Ruiz, S. M. Griffin, C. Jozwiak, Z. Chen, L.-W. Wang, A. M. Minor, M. Scott, A. G. Grushin, A. Lanzara, and F. Hellman, Observation of spin-momentum locked surface states in amorphous Bi$_2$Se$_3$, Nat. Mater. **22**, 200 (2023).

[48] H. Spring, A. R. Akhmerov, and D. Varjas, Amorphous topological phases protected by continuous rotation symmetry, SciPost Phys. **11**, 022 (2021).

[49] A. Agarwala, V. Juričić, and B. Roy, Higher-order topological insulators in amorphous solids, Phys. Rev. Res. **2**, 012067(R) (2020).

[50] J.-H. Wang, Y.-B. Yang, N. Dai, and Y. Xu, Structural-disorder-induced second-order topological insulators in three dimensions, Phys. Rev. Lett. **126**, 206404 (2021).

[51] T. Peng, C.-B. Hua, R. Chen, Z.-R. Liu, H.-M. Huang, and B. Zhou, Density-driven higher-order topological phase transitions in amorphous solids, Phys. Rev. B **106**, 125310 (2022).

[52] Y.-L. Tao, J.-H. Wang, and Y. Xu, Average symmetry protected higher-order topological amorphous insulators, SciPost Phys. **15**, 193 (2023).

[53] T. A. Loring and M. B. Hastings, Disordered topological insulators via C*-algebras, Europhys. Lett. **92**, 67004 (2011).

[54] R. Bianco and R. Resta, Mapping topological order in coordinate space, Phys. Rev. B **84**, 241106(R) (2011).

[55] G. Chang, S.-Y. Xu, B. J. Wieder, D. S. Sanchez, S.-M. Huang, I. Belopolski, T.-R. Chang, S. Zhang, A. Bansil, H. Lin, and M. Z. Hasan, Unconventional chiral fermions and large topological Fermi arcs in RhSi, Phys. Rev. Lett. **119**, 206401 (2017).

[56] D. A. Pshenay-Severin, Y. V. Ivanov, A. A. Burkov, and A. T. Burkov, Band structure and unconventional electronic topology of CoSi, J. Phys.: Condens. Matter **30**, 135501 (2018).

[57] F. de Juan, A. G. Grushin, T. Morimoto, and J. E. Moore, Quantized circular photogalvanic effect in Weyl semimetals, Nat. Commun. **8**, 15995 (2017).

[58] F. Flicker, F. de Juan, B. Bradlyn, T. Morimoto, M. G. Vergniory, and A. G. Grushin, Chiral optical response of multifold fermions, Phys. Rev. B **98**, 155145 (2018).

[59] D. Rees, K. Manna, B. Lu, T. Morimoto, H. Borrmann, C. Felser, J. E. Moore, D. H. Torchinsky, and J. Orenstein, Helicity-dependent photocurrents in the chiral Weyl semimetal RhSi, Sci. Adv. **6**, eaba0509 (2020).

[60] Z. Ni, B. Xu, M.-Á. Sánchez-Martínez, Y. Zhang, K. Manna, C. Bernhard, J. W. F. Venderbos, F. de Juan, C. Felser, A. G. Grushin, and L. Wu, Linear and nonlinear optical responses in the chiral multifold semimetal RhSi, npj Quantum Mater. **5**, 96 (2020).

[61] C. Guo, L. Hu, C. Putzke, J. Diaz, X. Huang, K. Manna, F.-R. Fan, C. Shekhar, Y. Sun, C. Felser, C. Liu, B. A. Bernevig, and P. J. W. Moll, Quasi-symmetry-protected topology in a semimetal, Nat. Phys. **18**, 813 (2022).

[62] L.-H. Hu, C. Guo, Y. Sun, C. Felser, L. Elcoro, P. J. W. Moll, C.-X. Liu, and B. A. Bernevig, Hierarchy of quasisymmetries and degeneracies in the CoSi family of chiral crystal materials, Phys. Rev. B **107**, 125145 (2023).

[63] A. Molinari, F. Balduini, L. Rocchino, R. Wawrzyńczak, M. Sousa, H. Bui, C. Lavoie, V. Stanic, J. Jordan-Sweet, M. Hopstaken, S. Tchoumakov, S. Franca, J. Gooth, S. Fratini, A. G. Grushin, C. Zota, B. Gotsmann, and H. Schmid, Disorder-induced magnetotransport anomalies in amorphous and textured $Co_{1-x}Si_x$ semimetal thin films, ACS Appl. Electron. Mater. **5**, 2624 (2023).

[64] T. A. Loring, K-theory and pseudospectra for topological insulators, Ann. Phys. **356**, 383 (2015).

[65] T. A. Loring, A guide to the Bott index and localizer index, arXiv:1907.11791.

[66] T. A. Loring and H. Schulz-Baldes, The spectral localizer for even index pairings, J. Noncommut. Geom. **14**, 1 (2020).

[67] H. Schulz-Baldes and T. Stoiber, Invariants of disordered semimetals via the spectral localizer, Europhys. Lett. **136**, 27001 (2021).

[68] H. Schulz-Baldes and T. Stoiber, Spectral localization for semimetals and Callias operators, J. Math. Phys. **64**, 081901 (2023).

[69] A. Cerjan and T. A. Loring, Local invariants identify topology in metals and gapless systems, Phys. Rev. B **106**, 064109 (2022).

[70] R. Zallen, *The Physics of Amorphous Solids* (Wiley-VCH, Weinheim, Germany, 1998).

[71] C.-T. Toh, H. Zhang, J. Lin, A. S. Mayorov, Y.-P. Wang, C. M. Orofeo, D. B. Ferry, H. Andersen, N. Kakenov, Z. Guo, I. H. Abidi, H. Sims, K. Suenaga, S. T. Pantelides, and B. Özyilmaz, Synthesis and properties of free-standing monolayer amorphous carbon, Nature (London) **577**, 199 (2020).

[72] P. Corbae, J. D. Hannukainen, Q. Marsal, D. Muñoz-Segovia, and A. G. Grushin, Amorphous topological matter: Theory and experiment, Europhys. Lett. **142**, 16001 (2023).

[73] S. T. Ciocys, Q. Marsal, P. Corbae, D. Varjas, E. Kennedy, M. Scott, F. Hellman, A. G. Grushin, and A. Lanzara, Establishing coherent momentum-space electronic states in locally ordered materials, arXiv:2302.05945.

[74] B. Xu, Z. Fang, M. Ángel Sánchez-Martínez, J. W. F. Venderbos, Z. Ni, T. Qiu, K. Manna, K. Wang, J. Paglione, C. Bernhard, C. Felser, E. J. Mele, A. G. Grushin, A. M. Rappe, and L. Wu, Optical signatures of multifold fermions in the chiral topological semimetal CoSi, Proc. Natl. Acad. Sci. USA **117**, 27104 (2020).

[75] See Supplemental Material at http://link.aps.org/supplemental/10.1103/PhysRevMaterials.8.L021201 for Bloch Hamiltonians of RhSi/CoSi and discuss how longer-range hoppings alter the band structure. We then show proofs of the existence of rare states in amorphous RhSi, before discussing in detail the spectral properties of the spectral localizer calculated for systems with double-Weyl fermions and threefold fermions. Finally, we discuss how our conclusions discussed in the main text differ in the case of a-CoSi.

[76] A. Weiße, G. Wellein, A. Alvermann, and H. Fehske, The kernel polynomial method, Rev. Mod. Phys. **78**, 275 (2006).

[77] M. Trescher, B. Sbierski, P. W. Brouwer, and E. J. Bergholtz, Tilted disordered Weyl semimetals, Phys. Rev. B **95**, 045139 (2017).

[78] E. Akkermans and G. Montambaux, *Mesoscopic Physics of Electrons and Photons* (Cambridge University, Cambridge, England, 2007).

[79] C. W. J. Beenakker, Random-matrix theory of quantum transport, Rev. Mod. Phys. **69**, 731 (1997).

[80] Y. Y. Atas, E. Bogomolny, O. Giraud, and G. Roux, Distribution of the ratio of consecutive level spacings in random matrix ensembles, Phys. Rev. Lett. **110**, 084101 (2013).

[81] Z.-Q. Zhang, B.-L. Wu, C.-Z. Chen, and H. Jiang, Global phase diagram of disordered higher-order Weyl semimetals, Phys. Rev. B **104**, 014203 (2021).

[82] S. Franca and A. G. Grushin, Obstructions in trivial metals as topological insulator zero-modes, arXiv:2304.01983.

[83] Q. Marsal, Topological phases in amorphous matter, Ph.D. thesis, Universite Grenoble Alpes, 2022.

[84] C. W. Groth, M. Wimmer, A. R. Akhmerov, and X. Waintal, Kwant: A software package for quantum transport, New J. Phys. **16**, 063065 (2014).

[85] S. Franca and A. G. Grushin, Topological diffusive metal in amorphous transition metal mono-silicides, https://doi.org/10.5281/zenodo.8095821 (2023).